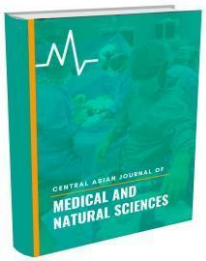

CENTRAL ASIAN JOURNAL OF MEDICAL AND NATURAL SCIENCES
https://cajmns.centralasianstudies.org/index.php/CAJMNS
Volume: 06 Issue: 02 | April 2025 ISSN: 2660-4159

.

Article

The Influence of Chemical Composition on The Shielding Coefficients for Different Materials to Gamma Rays and Fast Neutrons

Khalid Ahmed Ibrahim*[1], Sabah Mahmoud Aman Allah[2], Saif Amer Mahdi[3]

1,2,3. Department of Physics-College of Education for Pure Sciences-University of Kirkuk-Kirkuk-Iraq. College of Science, University of Tikrit
* Correspondence: ephm22005@uokirkuk.edu.iq

Abstract: Radiation shielding is critical in nuclear applications to protect human health and sensitive equipment from harmful ionizing radiation. The effectiveness of shielding materials depends on their chemical composition and interaction with gamma rays and fast neutrons. While various materials have been studied for radiation shielding, the selection and optimization of new alloys and concrete mixtures require precise computational and experimental analyses. Existing studies lack a comprehensive comparison of ternary metallic alloys and barite/goethite-based concrete mixtures for shielding both gamma rays and fast neutrons. The effectiveness of these materials under different radiation exposure conditions needs further investigation. This study aims to evaluate the shielding efficiency of selected ternary metallic alloys (Pb-Sb-Sn and Pb-Cu-Te) and barite/goethite-based concrete mixtures against gamma rays and fast neutrons using computational methods. The findings indicate that $Pb_{0.75}$-$Sb_{0.15}$-$Sn_{0.10}$ exhibits the highest attenuation for gamma rays, while barite-based concrete mixtures provide superior neutron shielding compared to dolomite-based mixtures. The study calculates key shielding parameters, including mass attenuation coefficients, mean free path, and half-value layer. Unlike conventional shielding materials, the study integrates computational tools such as XCOM and SAZ to provide a more precise evaluation of shielding performance, offering insights into material selection and design. These results contribute to the development of optimized shielding materials for nuclear applications, improving safety measures in industrial, medical, and research settings by enhancing material performance for radiation protection.

Keywords: Effective Atomic Number, Fast Neutron, Gamma Ray, Half, Tenth, Quarter, Layer, Mass Attenuation Coefficient, Molecular Cross-Section, NIST-XCOM, SAZ

Citation: Ibrahim, K. A., Allah, S. M. A., Mahdi, S. A. The Influence of Chemical Composition on The Shielding Coefficients for Different Materials to Gamma Rays and Fast Neutrons. Central Asian Journal of Medical and Natural Science 2025, 6(2), 762-774.

Received: 28th Feb 2025
Revised: 9th Mar 2025
Accepted: 15th Mar 2025
Published: 19th Mar 2025

1. Introduction

Nuclear technology is widely used in industry and medicine, but radiation from nuclear reactions poses risks to humans and equipment, requiring effective shielding materials [1], [2], [3]. Since gamma rays and neutrons interact differently with matter, understanding these interactions is crucial for evaluating shielding performance [4].

Gamma rays interact through three main mechanisms. At low energies, the photoelectric effect dominates, where a photon ejects an electron from an atom [5]. At intermediate energies, Compton scattering occurs, causing the photon to lose energy and

change direction [6]. At high energies (>1.022 MeV), pair production generates an electron-positron pair, while at energies above 2.044 MeV, triplet production occurs [7], [8].

Neutron interactions vary due to their wide energy range, making shielding complex [9]. Elastic scattering transfers energy to a nucleus, causing it to recoil [10]. Inelastic scattering excites the nucleus, leading to gamma emission [11]. In neutron capture, a nucleus absorbs a neutron and emits gamma radiation, requiring high atomic number materials to absorb secondary radiation effectively [12].

1.1 Gamma-Ray Attenuation Parameters:

The total mass attenuation coefficient (μ_t) (cm^2/g) is a measure of the probability of interactions occurring between incident photons and the thickness of the target material [13].

$$\mu_t = \frac{\mu}{\rho} \qquad (1)$$

Where μ (cm^{-1}) represents the linear attenuation coefficient, and ϱ (g/cm^3) denotes the material density [14].

The total molecular cross-section $\sigma_{t.m}$ (barn/molecule) is calculated using the following equation [15]:

$$\sigma_{t.m} = \mu_t \frac{M}{N_A} \qquad (2)$$

Where M represents the molecular weight, and N_a is Avogadro's number [15].

The total atomic cross-section (σ_t.a) (barn/atom) is calculated using the following equation [16]:

$$\sigma_{t.a} = \frac{\sigma_{t.m}}{\sum_i n_i} \qquad (3)$$

The total electronic cross-section (σ_t.e) (barn/electron) is calculated using the following equation [17]:

$$\sigma_{t.e} = \frac{1}{N_A} \sum_i f_i \frac{A_i}{Z_i} (\mu_t)_i \qquad (4)$$

Where f_i represents the weight fraction of each element in the compound.

The effective atomic number ($Z_e$ff) is calculated using the following equation [18]:

$$Z_{eff} = \frac{\sigma_{t.a}}{\sigma_{t.e}} \qquad (5)$$

The electron density (N_{ele}) is calculated using the following equation [19]:

$$N_{ele} = \frac{\mu_{t.m}}{\sigma_{t.e}} \qquad (6)$$

The mean free path (λ) (cm) is calculated using the following equation [20]:

$$\lambda = \frac{1}{\mu_t} \qquad (7)$$

The half-value layer HVL (cm), The tenth-value layer TVL (cm), and The quarter-value layer QVL (cm) are calculated using the following equations [21], [22], [23]:

$$HVL = \frac{ln(2)}{\mu_t} \qquad (8)$$

$$TVL = \frac{ln(10)}{\mu_t} \qquad (9)$$

$$QVL = \frac{ln(4)}{\mu_t} \qquad (10)$$

Neutrons Attenuation Parameters:

The effective cross-section for neutron removal (∑R) (cm^{-1}):

$\sum_R$ is defined as the probability that a fast neutron or a fission energy neutron undergoes its first collision, causing it to exit the group of penetrating neutrons that have not yet interacted. The ∑R computed using the following equation [24]:

$$\sum_R = \sum_i \rho_i (\frac{\sum_R}{\rho})_i \qquad (11)$$

Where ϱ_i is the partial density, and $\sum_R/\varrho$ (cm^2/g) represents the mass removal cross-section, which calculated semi-empirically using the following equations:

James Wood's equation [25] $\frac{\sum_R}{\rho} = 0.206A^{\frac{-1}{3}}.Z^{-0.294}$ (12)

Zoller's equation [26]: $\frac{\sum_R}{\rho} = 0.19Z^{-0.743} \quad Z \leq 8$ (13)

$$\frac{\sum_R}{\rho} = 0.125Z^{-0.565} \quad Z > 8 \qquad (14)$$

The half-value layer (HVL) (cm) and the mean free path (λ) (cm) calculated by using the following equations [27]:

$$HVL = \frac{ln(2)}{\sum_R} \qquad (15)$$

$$\lambda = \frac{1}{\sum_R} \qquad (16)$$

2. Materials and Methods

Shielding Materials Used

2.1 Shielding Materials Against Gamma Rays:

In this section, we used ternary copper alloys with different proportions, as shown in Table 1.

Table 1. The element proportions in each sample index study

Alloys	Samp.	%		
Pb – Sb – Sn	S 1	Pb = 0.60	Sb = 0.25	Sn = 0.15
	S 2	Pb = 0.70	Sb = 0.20	Sn = 0.10
	S 3	Pb = 0.75	Sb = 0.15	Sn = 0.10
Pb – Cu – Te	S 4	Pb = 0.60	Cu =0. 25	Te =0. 15
	S 5	Pb = 0.70	Cu = 0.20	Te = 0.10
	S 6	Pb = 0.75	Cu = 0.15	Te = 0.10

Natural gamma radiation sources were used, as shown in Table (2) and (3).

Table 2. Energies sources and their energies.

No.	Radioactive source	E (MeV)
1	241Am	0.05953
2	133Ba	0.08099
3	152Eu	0.1218
4		0.2447
5	133Ba	0.356
6	131I	0.364
7	137Cs	0.6617
8	152Eu	0.7789
9		0.9641
10	60Co	1.178
11		1.25
12		1.332
13	152Eu	1.408
14	24Na	2.75

Table 3. The density and molecular mass of the alloys under study.

Samp.	Denity of Samp.(g/cm^3)	Molecular Mass of Samp.
S 1	9.57475	172.5665
S 2	10.0084	181.263
S 3	10.24055	185.535
S 4	9.98	159.3475
S 5	10.354	170.51
S 6	10.473	177.6925

2.2 Shielding Materials Against Neutrons:

The same materials and mixture design as reported in the experimental study [28] were used, along with a theoretical computational analysis to evaluate their shielding effectiveness for neutrons. The studied mixtures included Barite-Limonite Concrete (BLC), which uses barite ($BaSO_4$) as coarse aggregate and limonite as fine aggregate, and Dolomite Concrete (DoC), which uses dolomite ($CaMg(CO_3)_2$) as coarse aggregate and silica sand as fine aggregate. The composition details and material ratios are provided in Tables (4) and (5).

Table 4. Concentrations content and density of the cementitious materials.

Oxide	Chemical Content (wt%)						
	PBFSC	SF	Barite	Dolomite	Limonite	Goethite	Sand
CaO	57.07	0.160	1.590	37.90	4.160	6.111	0.521
SiO_2	23.33	96.81	1.160	2.240	16.30	11.08	95.84
Al_2O_3	5.910	0.250	0.640	0.950	2.970	3.051	2.210
Fe_2O_3	3.290	0.450	20.84	0.610	68.10	62.30	0.820
MgO	3.100	0.260	1.630	15.03	0.650	0.893	0.101
MnO	--	0.050	1.100	--	--	0.263	--
SO_3	2.900	0.140	4.420	0.390	2.900	1.710	0.110
K_2O	0.250	0.280	0.340	0.070	0.740	1.620	0.690
Na_2O	0.240	0.140	--	0.250	0.990	1.314	0.270
TiO_2	0.080	--	--	0.130	1.290	1.341	0.120
BaO	--	--	67.10	--	--	--	--
Cr_2O_3	--	--	0.170	--	0.850	0.416	--

Density (g/cm³)	3.15	2.26	4.40	2.69	2.28	4.00	2.68

Table 5. Mixture ratios of the studied cement samples.

SAMP.	Concrete Mix Ratio (kg/m³)						
	Cement	Fine aggregates		Coarse aggregates			Pozzolans/ additives
	PBFSC	Sand	Limonite	Goethite	Barite	Dolomite	SF
BLC	450	270	226	--	1798	--	50
DoC	500	555	--	--	--	1126	--

3. Results and Discussion

3.1 Gamma Ray Attenuation Calculations:

In here the total mass attenuation coefficient ($\mu_{t,m}$) for the alloys under study were calculated using the XCOM database. calculates cross-sections for scattering processes, photoelectric absorption, pair production [29]. Table (6) presents the calculated values of the total mass attenuation coefficient (cm²/g) $\mu_{t,m}$ for gamma photon energies E (MeV), calculated using XCOM software.

Table 6. Total mass attenuation coefficient for the samples with photon energies.

E (MeV)	$\mu_{t.m}$ (cm²/g)					
	S 1	S 2	S 3	S 4	S 5	S 6
0.05953	5.834	5.66	5.565	4.558	4.63	4.804
0.08099	2.616	2.55	2.514	2.065	2.105	2.186
0.1218	2.444	2.679	2.795	2.268	2.536	2.69
0.2447	0.4671	0.5069	0.5266	0.443	0.4875	0.5123
0.356	0.2256	0.241	0.2487	0.2175	0.2346	0.2439
0.364	0.2172	0.2318	0.239	0.2096	0.2257	0.2346
0.6617	0.0964	0.09986	0.1016	0.0954	0.0991	0.101
0.7789	0.0819	0.08426	0.08543	0.0815	0.0839	0.0852
0.9641	0.0678	0.06923	0.06994	0.0678	0.0693	0.0699
1.178	0.0579	0.05886	0.0593	0.0582	0.0591	0.0594
1.25	0.0556	0.05639	0.05678	0.0558	0.0566	0.0569
1.332	0.0533	0.05406	0.05441	0.0536	0.0543	0.0546
1.408	0.0516	0.05227	0.05259	0.0519	0.0525	0.0527
2.75	0.0407	0.04122	0.04149	0.0405	0.0411	0.0413

In Figure 1, the total mass attenuation coefficient (μt) for the alloys under study is shown as a function of photon energy. As photon energy increases, μ_t associated with the photoelectric effect decreases. All selected alloys exhibit the same pattern, where the values of μ_t for this process increase with the atomic number of the material. This behavior can be explained by the nature of the photoelectric effect, which depends on the absorption of photons. The cross-section for the photoelectric effect is inversely proportional to the photon energy raised to the power of 3.5, while it is linearly proportional to the atomic number of the material raised to a specific power σ_ph∝Z^n/E^3.5 , where n=4→5. Based on this, the total mass attenuation coefficient increases when the material has a higher atomic number and decreases with increasing photon energy due to the reduced likelihood of interaction [30]. However, considering the absorption edge at 82 keV for the Pb-Sb-Sn alloy in samples (S1, S2, S3), we observe a decrease in the total mass attenuation coefficient with an increase in the weight percentage of lead (Pb) for energies lower than 82 keV, while it increases when the energy exceeds that value with the increasing Pb ratio.

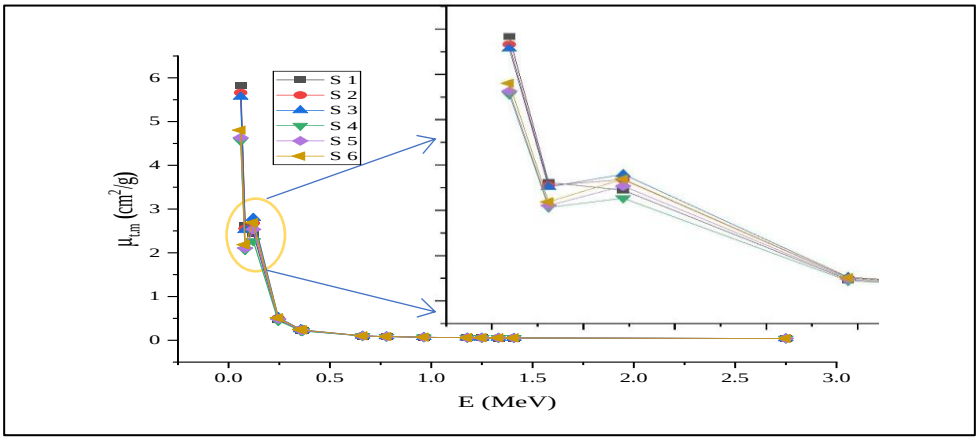

Figure 1. Total mass attenuation coefficient μ_t as a function of photon energy.

Table (7) Shows the total molecular cross-section $\sigma_{t,m}$ (barn/molecule) for the studied alloys under study, calculated using eq. (2) as a function of gamma photon energies (E) (MeV).

Table 7. the total molecular cross-section $\sigma_{t,m}$ as a function of gamma photon energies.

E (MeV)	$\sigma_{t.m}$ (*barn/molecular*)					
	S 1	**S 2**	**S 3**	**S 4**	**S 5**	**S 6**
0.05953	1671.5	1703.38	1714.27	1205.89	1310.74	1417.29
0.08099	749.52	767.426	774.423	546.327	595.922	644.921
0.1218	700.24	806.249	860.983	600.033	717.937	793.613
0.2447	133.83	152.552	162.216	117.202	138.01	151.14
0.356	64.637	72.5293	76.6106	57.5429	66.4148	71.9562
0.364	62.230	69.7605	73.6226	55.4528	63.8952	69.2125
0.6617	27.625	30.053	31.2973	25.2527	28.0579	29.7973
0.7789	23.468	25.3582	26.3162	21.562	23.7661	25.1271
0.9641	19.428	20.8349	21.5446	17.9428	19.6074	20.631
1.178	16.606	17.714	18.267	15.3924	16.7198	17.5332
1.25	15.930	16.9706	17.4907	14.776	16.0262	16.7927
1.332	15.288	16.2694	16.7607	14.1886	15.3722	16.0965
1.408	14.793	15.7307	16.2	13.7283	14.8627	15.5595
2.75	11.658	12.4052	12.7808	10.7043	11.6212	12.1963

Figure 2 Shows The relationship between the total molecular cross-section (σ_m) and photon energy, where its behavior is similar to that of the mass attenuation coefficient. The results show that the highest value of σ_m was sample S3, equal to 1714.27 Barn/molecule, based on calculations derived from equation (3). This behavior is attributed to the direct correlation between molecular cross-section and mass attenuation coefficient. A notable increase in $\sigma_{t,m}$ was observed at a photon energy of 0.05953 MeV due to the photoelectric effect. On the other hand, sample S4 was the lowest value for $\sigma_{t,m}$, which was 1205.89 Barn/molecule. This is explained by the lower density of the sample compared to the others and its higher proportion of copper, which has a lower atomic number compared to the other elements in the samples (Pb,Sb,Sn,Te).

It is worth noting that the atomic cross-section area $\sigma t._a$ exactly in agreement to the molecular cross-section area $\sigma t._m$. This agreement can be explained by the equation (3), where the denominator $\sum_{ni}$ in the case of alloys represents the sum of the proportions of the elements composing the alloy, which always equals one. As a result, $\sigma t._a$ and $\sigma t._m$ are equal, leading to identical results for both [31].

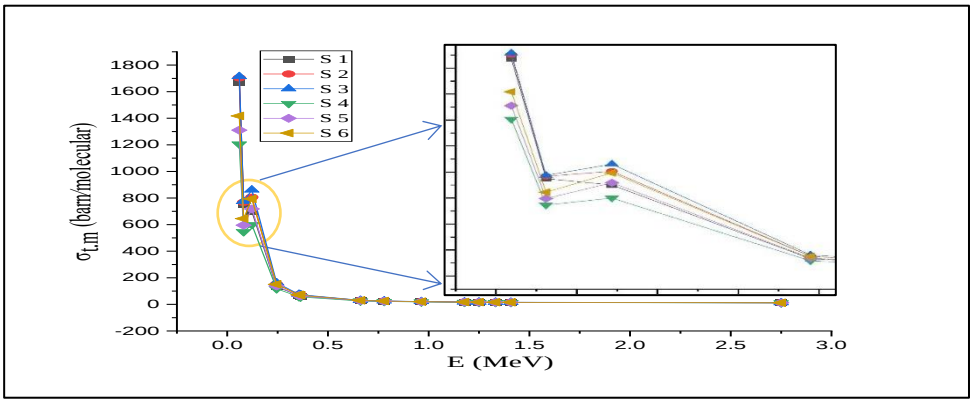

Figure 2. the total molecular cross-section σt.m as a function of photon energy.

Table (8) shows the values of the total electronic cross-section σele, obtained by using eq.(4), with the photon energies for the alloys being studied in gamma radiation attenuation.

Table 8. Electronic cross-section σele for the samples with photon energies.

E	σ_{ele} $(barn/electron)$					
(MeV)	S 1	S 2	S 3	S 4	S 5	S 6
0.05953	23.916	23.34	23.0066	18.4045	18.8524	19.6946
0.08099	10.724	10.5154	10.3933	8.33817	8.57112	8.96177
0.1218	10.019	11.0473	11.555	9.15785	10.3261	11.028
0.2447	1.9148	2.09029	2.17704	1.78877	1.985	2.10023
0.356	0.9248	0.99381	1.02816	0.87823	0.95524	0.9999
0.364	0.8904	0.95587	0.98806	0.84633	0.919	0.96177
0.6617	0.3953	0.41179	0.42003	0.38541	0.40356	0.41406
0.7789	0.3357	0.34746	0.35318	0.32909	0.34183	0.34916
0.9641	0.2780	0.28548	0.28914	0.27385	0.28201	0.28669
1.178	0.2376	0.24272	0.24516	0.23492	0.24048	0.24364
1.25	0.2279	0.23253	0.23474	0.22551	0.2305	0.23335
1.332	0.2187	0.22293	0.22494	0.21655	0.2211	0.22368
1.408	0.2116	0.21554	0.21742	0.20952	0.21377	0.21621
2.75	0.1668	0.16998	0.17153	0.16337	0.16715	0.16948

Figure 3 illustrates the variation in the total electronic cross-section σele as a function of incident photon energy. At low energies, its value is high, then it sharply decreases until it reaches a certain threshold, after which a slight increase occurs. It was observed that sample S3 has the highest value for σele after the absorption edge, while the lowest value was recorded for sample S4 at the same energy. This disagreement is attributed to the high (Z) for photon interactions in each alloy.

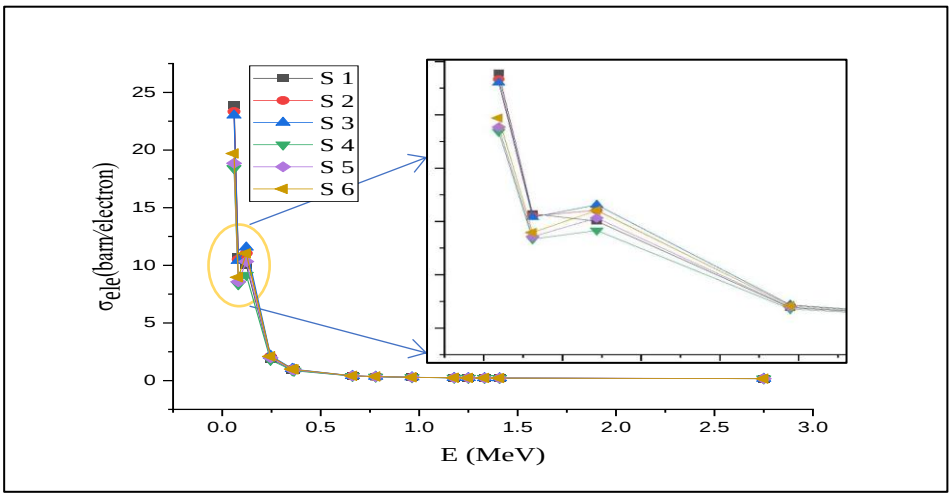

Figure 3. shows the effective atomic number Zeff, calculated using equation (5).

Zeff remains constant within the range of photon energies applied. The value of Zeff is determined by the chemical composition of the material, with the highest value was for sample S3, which equals 74.51 due to its high (Z). In contrast, the lowest value was found in sample S4, where it equals 65.521, due to the higher proportion of copper, an element with a lower atomic number compared to the other alloy elements.

Figure 5 displays the electronic density Nele, calculated using equation (6), which is related to the effective atomic number Zeff, indicating a fixed relationship with photon energy. The values of Nele vary among the studied compounds, with the highest values in the sample containing a high atomic number (Z) and the lowest values in the sample with fewer electrons. This variation is due to the effect of the relationship in equation (6).

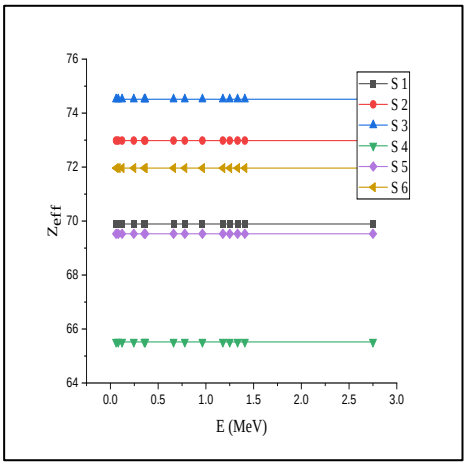

Figure 4. Shows the effective atomic number Zeff as a function of photon energy

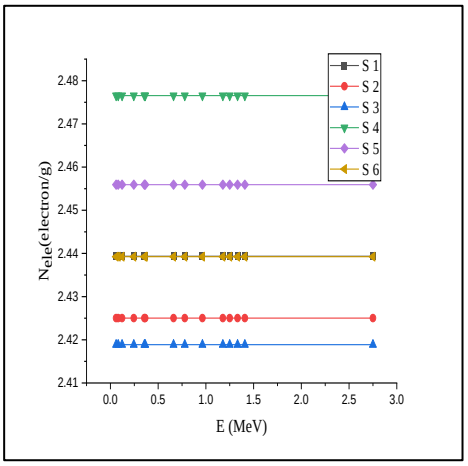

Figure 5. Shows the electronic density Nele as a function of photon energy.

Figure 6 shows the mean free path λ, calculated using equation (7). λ starts with a low value and then increases rapidly with the increase in photon energy, up its maximum value in sample S4. Afterward, it gradually decreases as the pair production reaction becomes dominant $\sigma_{p.p} \propto Z^2 \ln(E)$. In contrast, the lowest value of λ was recorded in sample S3 at the same energy. This is because sample S3 has a higher density and a higher effective atomic number compared to sample S4, which has a lower density and effective atomic number.

Figures 7, 8, 9 show the half-thickness HVL, tenth-thickness TVL, and quarter-thickness QVL, calculated using equations (8, 9, 10). It is observed that the values of HVL, TVL, and QVL are low at low photon energies, then start to increase with increasing photon energy, and stabilize at high energies when the pair production reaction becomes dominant. The highest values for these thicknesses were recorded in sample S4, while the lowest values found in sample S3, indicating higher absorption efficiency for this sample. The difference in values is attributed to the density of the samples and their composition of elements with varying atomic numbers.

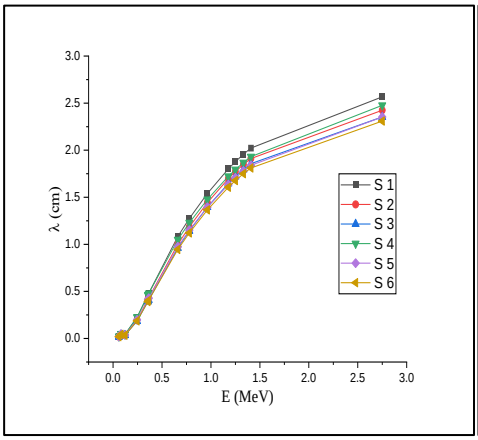

Figure 6. Shows the λ as a function of photon energy.

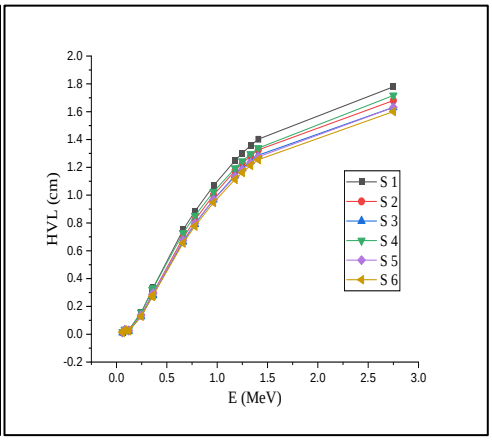

Figure 7. Shows the HVL as a function of photon energy.

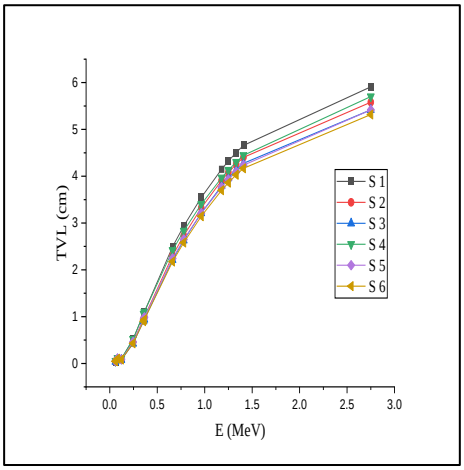

Figure 8. shows the TVL as a function of photon

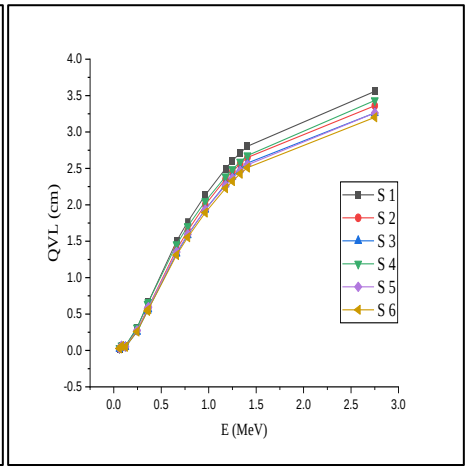

Figure 9. Shows the QVL as a function of photon energy.

3.2 Fast Neutron Calculations:

From Table (5), the weight fraction of each cementitious mixture in both BLC and DoC was calculated, as shown in Table (9).

Table 9. Weight fraction of cementitious materials in the two samples.

SAMP.	Weight Fraction %						
	PBFSC	Sand	Limonite	Barite	Dolomite	SF	Total
BLC	0.161	0.09663	0.0809	0.6435	0	0.0179	1
DoC	0.229	0.25447	0	0	0.5162769	0	1

Tables 10, 11 show the weight fraction of compounds in both BLC and DoC, calculated based on Tables (4) and (9).

Table 10. Volume fraction of compounds in the BLC sample.

	Comp.	PBFSC	SF	Barite	Limonite	Sand
BLC	**CaO%**	0.0918827	0.00002864	0.01023165	0.00336544	0.000503442
	SiO_2%	0.0375613	0.01732899	0.0074646	0.0131867	0.092610192
	Al_2O_3%	0.0095151	0.00004475	0.0041184	0.00240273	0.002135523
	Fe_2O_3%	0.0052969	0.00008055	0.1341054	0.0550929	0.000792366
	MgO%	0.004991	0.00004654	0.01048905	0.00052585	9.75963E-05
	MnO%	0	0.00000895	0.0070785	0	0
	SO_3%	0.004669	0.00002506	0.0284427	0.0023461	0.000106293
	K_2O%	0.0004025	0.00005012	0.0021879	0.00059866	0.000666747
	Na_2O%	0.0003864	0.00002506	0	0.00080091	0.000260901
	TiO_2%	0.0001288	0	0	0.00104361	0.000115956
	BaO%	0	0	0.4317885	0	0
	Cr_2O_3%	0	0	0.00109395	0.00068765	0

Table 11. Volume fraction of compounds in the DoC sample.

	Comp.	PBFSC	Dolomite	Sand
DoC	**CaO%**	0.1306903	0.195668945	0.001325789
	SiO_2%	0.0534257	0.011564603	0.243884048
	Al_2O_3%	0.0135339	0.004904631	0.005623787
	Fe_2O_3%	0.0075341	0.003149289	0.002086654
	MgO%	0.007099	0.077596418	0.000257015
	SO_3%	0.006641	0.00201348	0.000279917
	K_2O%	0.0005725	0.000361394	0.001755843
	Na_2O%	0.0005496	0.001290692	0.000687069
	TiO_2%	0.0001832	0.00067116	0.000305364

Attenuation parameters for certain fast neutrons of the BLC and DoC samples were calculated, along with the calculated of the partial density and weight fraction of each element in each sample, as shown in Tables (12, 13).

The effective cross-section for neutron removal (ΣR) was calculated as shown in tables (12, 13), and the results showed a significant agreement between the BLC and DoC samples with the experimental data presented in the study [28]. Despite the higher density of the BLC mixture, its efficiency in shielding fast neutrons was lower compared to the DoC mixture. This is due to the lower content of light elements in BLC, despite its higher content of heavy elements. Light elements play a key role in slowing down fast neutrons and converting them into thermal neutrons through elastic scattering processes. These results highlight the importance of carefully selecting concrete components to ensure the formation of an effective matrix capable of absorbing various elements, contributing to an integrated level of protection against diverse radiations.

Table (14) shows the values of the mean free path (λ), which is inversely related to ΣR, and the lowest λ value was recorded for the DoC sample, which is attributed to its higher density, while the highest value was for the BLC sample due to its lower bulk density. These values also showed significant agreement with the data published in reference [28].

Additionally, Table (14) presents the values of the half-value layer (HVL), which exhibited similar behavior to the mean free path, with a significant agreement with the experimental results from the study [29].

The slight differences between the theoretical and experimental results can be explained by considering manufacturing defects, voids inside the samples, as well as the presence of trace oxide impurities [30. Additionally, the volatilization of some atoms during the manufacturing process may also contribute to this discrepancy [31]. All these factors lead to a slight variation between the calculated and experimental values.

Table 12. Elements of the BLC sample with volume fraction, partial density, ∑R/ ϱ, and ΣR for each element.

SAMP.	Ele.	Element %	ρ_P (g/cm³)	$\sum_R/\rho$ (cm²/g)		$\sum_R$ (cm⁻¹)		
				Wood	Zoller	Wood	Zoller	EXP.[28]
BLC	O	0.267013	1.020630491	0.04436	0.040528	0.045275169	0.041364113	
	Na	0.001106	0.004227574	0.03579	0.03225	0.000151305	0.000136339	
	Mg	0.009874	0.037742378	0.0344	0.0307	0.001298338	0.001158691	
	Al	0.009659	0.036920562	0.032303	0.0293448	0.001192645	0.001083426	
	Si	0.079619	0.304335666	0.031226	0.0281415	0.009503185	0.008564462	
	S	0.014456	0.055256614	0.028717	0.0260965	0.001586804	0.001442004	
	K	0.003283	0.012548939	0.02556	0.0236817	0.000320751	0.00029718	
	Ca	0.076809	0.293594722	0.0249657	0.023005	0.007329798	0.006754147	
	Ti	0.000784	0.002996762	0.02284447	0.0218	6.84594E-05	6.53294E-05	
	Cr	0.001249	0.004774178	0.02168	0.07534	0.000103504	0.000359687	
	Mn	0.005575	0.02130988	0.0209	0.02028	0.000445376	0.000432164	
	Fe	0.138283	0.528572939	0.0205387	0.019835	0.010856201	0.010484244	
	Ba	0.392292	1.499496941	0.0122365	0.012858	0.018348594	0.019280532	
Total		1	3.8224	0.04436	0.040528	0.09648013	0.091422319	0.103

Table 13. Elements of the DoC sample with volume fraction, partial density, ∑R/ ϱ, and ΣR for each element.

SAMP.	Ele.	Element %	ρ_P (g/cm³)	$\sum_R/\rho$ (cm²/g)		$\sum_R$ (cm⁻¹)		
				Wood	Zoller	Wood	Zoller	EXP.[28]
DoC	O	0.405614	1.132474288	0.04436	0.040528	0.050236559	0.045896918	
	Na	0.002423	0.006765016	0.03579	0.03225	0.00024212	0.000218172	
	Mg	0.066217	0.184877864	0.0344	0.0307	0.006359799	0.00567575	
	Al	0.016461	0.045959112	0.032303	0.0293448	0.001484617	0.001348661	
	Si	0.186619	0.521040248	0.031226	0.0281415	0.016270003	0.014662854	
	S	0.004625	0.012913	0.028717	0.0260965	0.000370823	0.000336984	
	K	0.002886	0.008057712	0.02556	0.0236817	0.000205955	0.00019082	
	Ca	0.30271	0.84516632	0.0249657	0.023005	0.021100169	0.019443051	
	Ti	0.000899	0.002510008	0.02284447	0.0218	5.73398E-05	5.47182E-05	
	Fe	0.011545	0.03223364	0.0205387	0.019835	0.000662037	0.000639354	
Total		1	2.792			0.096989421	0.088467283	0.108

Table 14. Values of ΣR, HVL, and λ for the studied samples.

SAMP.	$\sum_R$ (cm⁻¹)			HVL (cm)			λ(cm)		
	Wood	Zoller	EXP.[28]	Wood	Zoller	EXP.[28]	Wood	Zoller	EXP.[28]
BLC	0.09648013	0.091422319	0.103	7.184	7.582	6.729	10.365	10.938	9.708
DoC	0.097	0.0885	0.108	7.147	7.835	6.478	10.310	11.304	9.259

4. Conclusion

In this study, the gamma-ray attenuation properties of a set of alloys listed in table (1) were examined based on the NIST-XCOM database. The results showed that sample (S3) exhibited the highest attenuation coefficients against gamma rays due to its higher concentration of lead compared to the other alloys, which possesses high density and a large atomic number, in addition to containing other elements with relatively high atomic numbers. Neutron attenuation parameters for the concrete samples BLC and DoC were also analyzed to assess their ability to reduce the impact of fast neutrons using a semi-empirical equation-based program. By calculating the ΣR values for the samples through the SAZ code, it was found that sample DoC recorded the highest value compared to sample BLC, which aligns with the results of the experimental study, indicating that it is more suitable for use in designing shields specifically for neutron protection in various applications.

REFERENCES

[1] N. J. AbuAlRoos, N. A. B. Amin, and R. Zainon, "Conventional and new lead-free radiation shielding materials for radiation protection in nuclear medicine: A review," *Radiation Physics and Chemistry*, vol. 165, p. 108439, 2019.

[2] B. Gan et al., "Research progress of metal-based shielding materials for neutron and gamma rays," *Acta Metallurgica Sinica (English Letters)*, vol. 34, no. 12, pp. 1609-1617, 2021.

[3] B. Aygün et al., "Development of new heavy concretes containing chrome-ore for nuclear radiation shielding applications," *Progress in Nuclear Energy*, vol. 133, p. 103645, 2021.

[4] D. A. Kahraman, F. T. Cogalmis, A. N. Esen, S. Haciyakupoglu, and B. F. Senkal, "Neutron and gamma-ray shielding effectiveness of novel polyaniline composites," *Radiation Physics and Chemistry*, vol. 219, p. 111675, 2024.

[5] D. Giovagnoli, "Image reconstruction for three-gamma PET imaging," Doctoral dissertation, Ecole nationale supérieure Mines-Télécom Atlantique, 2020.

[6] M. Ragheb, "Gamma rays interaction with matter," *Nuclear, Plasma and Radiation Science. Inventing the Future*, pp. 17-22, 2011. [Online]. Available: https://netfiles.uiuc.edu/mragheb/www.

[7] T. Olsen et al., "Radiation effects on materials for electrochemical energy storage systems," *Physical Chemistry Chemical Physics*, vol. 25, no. 45, pp. 30761-30784, 2023.

[8] G. O. Depaola, M. L. Iparraguirre, and D. Palacios, "About electrons and position in Triplet Production: some remarks," *Physics Open*, vol. 5, p. 100044, 2020.

[9] A. Martin, S. Harbison, K. Beach, and P. Cole, *An introduction to radiation protection*, CRC Press, 2018.

[10] P. Rinard, "Neutron interactions with matter," in *Passive nondestructive assay of nuclear materials*, 1991, pp. 375-377.

[11] Z. M. Nuri, A. A. Aziz, and S. M. A. Allah, "Investigation of the Protective Armours for Gamma Rays and Fast Neutrons Parameters," *Nanotechnology Perceptions*, pp. 546-560, 2024.

[12] T. E. Johnson, *Introduction to health physics*, McGraw Hill Professional, 2017.

[13] B. Tellili, Y. Elmahroug, and C. Souga, "Investigation on radiation shielding parameters of cerrobend alloys," *Nuclear Engineering and Technology*, vol. 49, no. 8, pp. 1758-1771, 2017.

[14] M. Maqbool, "Interaction of gamma rays and X-rays with matter," in *An Introduction to Medical Physics*, pp. 43-61, 2017.

[15] B. Akça and S. Z. Erzeneoğlu, "The mass attenuation coefficients, electronic, atomic, and molecular cross sections, effective atomic numbers, and electron densities for compounds of some biomedically important elements at 59.5 keV," *Science and Technology of Nuclear Installations*, vol. 2014, p. 901465, 2014.

[16] S. R. Manohara, S. M. Hanagodimath, K. S. Thind, and L. Gerward, "On the effective atomic number and electron density: a comprehensive set of formulas for all types of materials and energies above 1 keV," *Nuclear Instruments and Methods in Physics Research Section B: Beam Interactions with Materials and Atoms*, vol. 266, no. 18, pp. 3906-3912, 2008.

[17] B. Koirala et al., "Cancer radiotherapy based on attenuation coefficient," *International Journal of Research and Innovation in Applied Science*, vol. 6, no. 12, pp. 21-24, 2021.

[18] A. M. Alqahtani et al., "Study of ionizing radiation attenuation of glass as: gamma rays shielding material," *Chalcogenide Letters*, vol. 19, no. 4, 2022.

[19] V. Jalal, "The dependence of X-ray attenuation parameters of (Al, Cu, and Zr) metals on their atomic number," *Available at SSRN*, vol. 4392990, 2023.

[20] B. V. Kheswa, "Gamma radiation shielding properties of (x) BiO–(0.5–x) ZnO–0.2 BO–0.3 SiO glass system," *Nukleonika*, vol. 69, no. 1, pp. 23-29, 2024.

[21] I. S. Mustafa, N. A. N. Razali, A. R. Ibrahim, N. Z. Yahaya, and H. M. Kamari, "From rice husk to transparent radiation protection material," *Jurnal Intelek*, vol. 9, no. 2, pp. 1-6, 2016.

[22] B. V. Kheswa, S. N. T. Majola, and S. N. Majola, "Impact of Bi2O3 on the X-ray shielding characteristics of telluro-borate-bismuth glass for medical applications," *Journal of Theoretical and Applied Physics*, vol. 18, no. 3, 2024.

[23] S. A. Al-Shelkamy, H. M. Hashish, and E. Salama, "Radiation attenuation, structural, mechanical and lubricant wear analysis against 5% wt. NaCl of heat treated stainless steel grades," 2021.

[24] A. E. S. Abdo, "Calculation of the cross-sections for fast neutrons and gamma-rays in concrete shields," *Annals of Nuclear Energy*, vol. 29, no. 16, pp. 1977-1988, 2002.

[25] K. H. S. Abdullah and S. A. Mahmod, "Calculation the fast neutrons interaction parameters for several carbohydrates," *Stallion Journal for Multidisciplinary Associated Research Studies*, vol. 3, no. 2, pp. 56-62, 2024.

[26] A. El Abd, G. Mesbah, N. M. Mohammed, and A. Ellithi, "A simple method for determining the effective removal cross section for fast neutrons," *J. Radiat. Nucl. Appl.*, vol. 2, no. 2, pp. 53-58, 2017.

[27] M. A. H. Abdullah et al., "Recent trends in advanced radiation shielding concrete for construction of facilities: materials and properties," *Polymers*, vol. 14, no. 14, p. 2830, 2022.

[28] I. M. Nabil et al., "Experimental, analytical, and simulation studies of modified concrete mix for radiation shielding in a mixed radiation field," *Scientific Reports*, vol. 13, no. 1, p. 17637, 2023.

[29] H. Nulk, "Computional investigation of gamma shielding behaviour of cementbasalt composite for nuclear energy applications," Tartu: Tartu Ülikool, 2014.

[30] A. Ali et al., "A comparative study of gamma radiation shielding parameters for sodium silicate glass containing bismuth, barium and lead oxide in the energy range (0.6–1.5 MeV)," *Wadi Alshatti University Journal of Pure and Applied Sciences*, vol. 2, no. 1, pp. 16-22, 2024.

[31] T. Singh, A. Kaur, J. Sharma, and P. S. Singh, "Gamma rays' shielding parameters for some Pb-Cu binary alloys," *Engineering Science and Technology, An International Journal*, vol. 21, no. 5, pp. 1078-1085, 2018.